Journal of The Electrochemical Society

OPEN ACCESS

Unveiling the Interplay of Structural and Electrochemical Degradation of $LiNi_{0.85}Mn_{0.05}Co_{0.05}O_2$ Cathode Material for Li-Ion Batteries

To cite this article: D. Goldbach *et al* 2024 *J. Electrochem. Soc.* **171** 080521

Journal of The Electrochemical Society, 2024 **171** 080521

Unveiling the Interplay of Structural and Electrochemical Degradation of $LiNi_{0.85}Mn_{0.05}Co_{0.05}O_2$ Cathode Material for Li-Ion Batteries

D. Goldbach,[1,2] J. Gluch,[3] M. Gaus,[1] T. Graf,[1] S. Käbitz,[1] and U. Krewer[2,z]

[1]*Volkswagen AG, Niedersachsen, 38239 Salzgitter, Germany*
[2]*Institute for Applied Materials - Electrochemical Technologies, Karlsruhe Institute of Technology, 76131 Karlsruhe, Germany*
[3]*Fraunhofer Institute for Ceramic Technologies and Systems IKTS, 01109 Dresden, Germany*

Nickel-rich layered oxides, crucial for high-energy-density Li-ion batteries, face challenges in cycle life due to intricate chemo-mechanical degradation. This study pioneers a comprehensive approach, integrating nano X-ray computed tomography and advanced electrochemical methods, to untangle the interplay of degradation mechanisms in complex composite electrodes. The evolution of cracking in Nickel-rich cathodes is meticulously quantified under diverse operating conditions. Surprisingly, our findings unveil that, contrary to conventional wisdom, crack formation is not the primary driver of capacity decay in Nickel-rich cathodes. Instead, the limiting factor emerges from the interplay between cycling-induced cracks and a progressively growing resistivity. Cracks, amplifying electrochemically active surfaces, foster side reactions, elevating resistance, and consequently diminishing capacity and current rate capability. This novel insight redirects attention to the dynamic resistivity growth, pinpointing operating conditions as a critical contributor. This work not only advances our understanding of Nickel-rich cathode degradation but also provides a framework for strategic mitigation strategies.
 [DOI: 10.1149/1945-7111/ad6a8f]

Manuscript submitted May 16, 2024; revised manuscript received July 3, 2024. Published August 20, 2024.

Supplementary material for this article is available online

The increasing demand for energy storage solutions, driven by the proliferation of intelligent mobile devices, grid-level energy storage, and electric vehicles, has intensified the quest for advanced lithium-ion batteries (LIBs) that embody rapid charging, high capacity, and extended lifetime.[1,2] Nickel-rich layered Lithium-Nickel-Manganese-Cobalt-Oxides (NMC) with a nickel content of more than 80 wt% have emerged as front-runners as active cathode materials (CAMs) for the next generation of LIBs, boasting superior specific capacity, power capabilities, cost efficiency, and reduced cobalt reliance.[3–6]

Despite these merits, Ni-rich cathode materials suffer from structural instability, resulting in inadequate operational lifetimes, particularly when subjected to high cut-off voltages essential for fully unlocking their high energy density potential.[7,8] This challenge manifests as a multifaceted issue involving several degradation mechanisms. The capacity loss occurs due to transition metal migration to lithium storage sites during cycling,[9–13] electrode cross-talk results from the dissolution of transition metals.[14] Additionally, surface structure of the CAM changes from layered structures to spinel-type and rock-salt like surface layers.[15,16] An additional layer of complexity is introduced by intergranular cracking, a consequence of considerable anisotropic volume changes during highly delithiated states.[16] This intricate degradation process is further exacerbated by gas evolution, a result of Ni^{4+} reactivity with conventional electrolytes, occurring at charge levels similar to lattice collapse.[17–20]

Among the myriad degradation mechanisms outlined, intergranular cracking has been underscored as a paramount concern requiring attention.[21–26] It has been found that the significant expansion and contraction of the c-lattice parameter during cycling induces stress on the cathode secondary particles, potentially leading to the development of micro-cracks along the grain boundaries of primary particles.[27] This phenomenon primarily occurs during high-voltage cycling and is associated with pronounced and abrupt anisotropic volume changes, specifically related to the H2-H3 phase transition.[28,29] The subsequent intergranular fracture can lead to the formation of microcracks, exposing the interior of the particle to electrolyte penetration. This increased CAM-to-electrolyte interface area, situated at a high cathode potential, can expedite parasitic side reactions, including solvent corrosion,[30] salt depletion,[31] and increase surface degradation of the CAM.[19,32–35] Continued operation may result in impedance rise[36,37] and electrical disconnection of Li storage sites within the CAM,[11,21–23] potentially reducing the battery's operational lifespan. These challenges pose substantial hurdles to the widespread adoption of Ni-rich cathode materials, emphasizing the critical need for comprehensive strategies to mitigate intergranular cracking and its subsequent effects in order to advance the practical applications. When the material is highly delithiated, the H2-H3 phase transition occurs accompanied by severe lattice collapse along the c-direction, ultimately leading to unit volume shrinkage. Consequently, cracks gradually propagate within the secondary particles, resulting in mechanical failure.

Numerous strategies have been proposed to address challenges associated with Ni-rich cathode materials. A promising approach to combat degradation is the targeted stabilization of the electrode-electrolyte interface, which is achieved through the use of electrolyte additives,[38,39] the application of surface coatings to the CAM particles,[40] or the adoption of a core–shell design for particles. In the core–shell-design, a core with high Ni content is encased in a Ni-depleted outer shell to minimize side reactions at the electrode-electrolyte interface.[41] An additional approach is to enhance the structural integrity by doping, a technique proven to mitigate the formation of microcracks within CAM particles during highly delithiated states.[42,43]

As the demand for improved battery performance and longevity increases, understanding the role and origins of cracking in Ni-rich CAM is essential for developing preventive measures and extending battery life. Previous studies have made progress in showcasing crack propagation within secondary particles, employing techniques such as destructive focused ion beam scanning electron microscopy, high-resolution X-ray computed tomography, and lower resolution X-ray CT. Despite these efforts, a significant research gap persists in comprehending the specific impact and intricate interplay of these cracks with electrochemical loss processes. While existing experiments hint at a general increase in impedance and capacitance loss, a

[z]E-mail: ulrike.krewer@kit.edu

nuanced exploration of these effects is absent. Additionally, there is a notable lack of quantitative analyses focusing on particle cracking under diverse operating conditions, especially those pertinent to commercial LIB cells. Filling these gaps is pivotal for advancing our understanding of the performance and degradation of Ni-rich CAM and underscores the necessity for a comprehensive investigation of the quantitative aspects of particle cracking into the complex interactions with electrochemical loss processes in various battery operation scenarios relevant for real-world applications.

In scientific discourse, capacity loss and impedance increase are generally attributed to isolated degradation processes like surface reconstruction, transition metal migration, or particle cracking. Contrary to this prevailing paradigm, our work challenges it by exploring the intricate interplay of particle cracking, the mechanism currently recognized as holding the dominant role, and acknowledging that the interactions between different processes may be equally or even more important than the individual processes alone. This study represents a novel exploration, as the complex interactions of particle cracking across different aging states and operational conditions are still largely unexplored. Our main focus is to elucidate the structural degradation of CAM, and its subtle influence on individual overpotential-causing loss processes that affect the capacity retention of polycrystalline Ni-rich layered NMC composite electrodes in different aging states. Through a nuanced differentiation in the discussion concerning structural degradation, specifically distinguishing from CAM fragmentation due to particle cracking from surface reconstruction, we individually correlate the influence of each process on electrochemical performance metrics. Employing experiments with varied cycle numbers, current rates (C-rates), temperatures, and charging protocols, we aim to capture snapshots of the cathode's condition during cyclic aging and diverse operational scenarios. Utilizing nanoscale X-ray computed tomography (Nano-XCT) scans, we quantify and visualize the physical crack density in CAM particles with high spatial resolution, enabling a meticulous examination of the microstructure's evolution. What sets our study further apart is the breakdown of total overpotential into individual processes, achieved through a combination of impedance and pulse measurements for positive electrodes. To the best of our knowledge, this represents the first comprehensive study of its kind, systematically and quantitatively examining the interaction between structural and electrochemical degradation for various operational conditions. Based on the insights gained from this study, recommendations are put forth as exemplary measures for optimizing electrode design and operational strategies. These proposals aim to strike a balance between harnessing the advantages of high energy density and fulfilling the requirement for an extended operational lifetime. The overall aim is to establish a comprehensive framework guiding research endeavors, providing an objective evaluation of strategies to mitigate deterioration in electrochemical performance and mechanical integrity. This quantitative foundation aims to inform decision-making in current and future optimization approaches for CAM in advanced material and electrode development.

Experimental

Materials.—The CAM utilized in this study was polycrystalline NMC811 obtained from the commercial supplier Novonix Ltd, Canada. It was provided in the form of electrode sheets with a loading of approximately 14.2 mg CAM cm^{-2} and exhibited a specific capacity of 211.3 mAh g^{-1}, translating to ≈3.0 mAh cm^{-2}. The precise composition was $Li_1Ni_{0.85}Mn_{0.05}Co_{0.1}O_2$. The particle size distribution of the active material is characterized by a d10 of 6.3 μm, a median particle size (d50) of 11.36 μm, and a d90 of 19.15 μm. The electrode sheets, coated on one side, had a thickness of 66 μm, including an 18 μm aluminum current collector. Cathodes of 18 mm diameter were punched out of these electrode sheets with an EL-Cut from EL-Cell and subsequently dried at 150 °C in a Büchi Glasofen B-585 under vacuum conditions overnight.

Testing equipment.—All experiments were executed using three-electrode PAT cells supplied by EL-Cell, utilizing the PAT core system to minimize human-induced variations in the experimental setup. Cell assembly was carried out in an argon-filled glove box (MBraun, $H_2O < 0.1$ ppm, $O_2 < 0.1$ ppm) using metallic lithium foil (300 μm thickness and 18 mm diameter, 99.9%, Rockwood Lithium) as the counter-electrode and a Whatman GF glass fiber separator (uncompressed thickness = 260 μm). 200 μL of BASF LP30 (1 mol l^{-1} $LiPF_6$ and ethylene carbonate/dimethyl carbonate (EC: DMC, 50:50 wt%)) with 2 wt% vinylene carbonate was used as electrolyte. The glass fiber separator, combined with a substantial electrolyte volume, functioned as an electrolyte reservoir. The Li-metal anode ensured an excess of lithium (Li), attributing observed cell aging solely to cathode degradation. Subsequently, the cells were transferred to a PAT-Tester-i-16 from EL Cell, featuring cableless connections between the test cell and potentiostat for electrochemical impedance spectroscopy (EIS) and cell testing within a temperature-controlled chamber. The inclusion of the reference electrode allowed for a precise determination of the impedance and potential response of the positive electrode, referred to hereafter as the working electrode.

Electrochemical measurements.—All cells were subjected to an identical characterization procedure, both before and after cycle testing at an ambient temperature of 25 °C. Throughout the characterization and the entire cycling test, the potential of the working electrode, denoted as $E_{cathode}$ in subsequent discussions, was controlled and monitored against the reference electrode. The C-rate was set to 1C ≡ 2.86 mA cm^{-2} and the operational voltage window for the working electrode was set to 3.0–4.35 V against Li^+/Li. The protocol began with a 6 h open circuit voltage (OCV) phase to ensure complete wetting of the electrodes. To ensure reliable results, measurements were conducted in duplicate for each condition. All cells underwent an initial three-cycle CC–CV/CC (constant current (CC), constant voltage (CV)) formation process, sustaining a constant current density of 0.286 mA cm^{-2} (∼C/10 rate) and concluding with a cut-off current of 0.143 mA cm^{-2} (∼C/20 rate) at the end of the CV charge phase. The discharge capacity of the third cycle served as the reference capacity. Additionally, a slow discharge capacity test at a low C-rate of C/20 was performed. Subsequently, cells were brought to 50% state of charge (SOC) at C/20, followed by a three-hour idle period. Galvanostatic electrochemical impedance spectroscopy (GEIS) and direct current internal resistance (DCIR) measurements were conducted, with GEIS data collected at OCV from 100 kHz to 1 mHz with an amplitude of 200 mA. For DCIR tests, a pulse current step with a height of 1.43 mA cm^{-2} (∼C/2 rate) and a duration of 180 s was executed. The DCIR value was calculated as the quotient of the difference of the last potential signal during the pulse current step ($E_c(t_{end})$) and the open circuit potential three hours after the pulse current step ($E_c^0 = E_c(t_{3h\ relaxed})$), divided by the pulse current (see Eq. 1).

$$R_{\mathrm{DCIR}} = \frac{E_c^0 - E_c(t_{end})}{I_{pulse}} \qquad [1]$$

The standard C-rate employed during the cycle test was set at 1.43 mA cm^{-2} (∼C/2 rate). In test series where the C-rate deviated from C/2 during cycle testing, an additional discharge at C/2 was conducted in the final characterization to facilitate a comparison of rate capability between test series. At the conclusion of each charging cycle, a CV step was executed with a low cut-off current of 0.143 mA cm^{-2} (∼C/20 rate). This step was designed to mitigate lithium concentration variations within the electrode, ensuring uniform utilization of the entire CAM. To comprehensively assess mechanical degradation within the CAM and its impact on electrochemical performance parameters across different aging states, experiments involving varying cycle numbers were carried out. The purpose of this approach was to capture snapshots of the

cathode's condition throughout the cyclic aging process for subsequent in-depth analysis. Further investigations delved into evaluating potential effects of aging modes, including C-rate variation, elevated temperature during cycling, and the omission of the constant voltage charging phase at the end of each charging cycle. Detailed specifications of all cyclic aging tests are provided in Table I.

Following the completion of electrochemical measurements, cells were discharged to 3.0 V and then disassembled within a glove box. The positive electrodes were extracted and cleansed with dimethyl carbonate to eliminate solvent and conductive salt residues. Subsequently, the electrodes underwent post-mortem analysis using nano X-ray computed tomography.

Method for quantifying loss processes.—The approach employed for quantifying individual loss processes is rooted in the methodology outlined by,[44] with modifications tailored for characterizing the working electrode in a three-electrode configuration and Li metal as the counter electrode. During battery operation, the operating potential (E_c) derived from the open circuit potential (E_c^0) and the summation of individual overpotentials η_i. E_c is calculated according to Eq. 2, where the total overpotential η during charging is added to E_c^0 and subtracted during discharging.

$$E_c = E_c^0 \pm \sum_i \eta_i \qquad [2]$$

Considering all loss contributions η_i to the total overpotential η, Eq. 2 can be expressed as

$$E_c = E_c^0 \pm \eta_0 \pm \eta_{c.c.,c} \pm \eta_{ct,c} \pm \eta_{film,c} \pm \eta_{diff,c} \pm \eta_{diff,e} \qquad [3]$$

Here, η_0 represents ohmic and ionic losses, $\eta_{c.c.,c}$ denotes contact loss at the working electrode, $\eta_{ct,c}$ and $\eta_{film,c}$ refer to interface losses for charge transfer at the working electrode and film transport, respectively, $\eta_{diff,c}$ signifies diffusion losses in the solid and $\eta_{diff,e}$ in the electrolyte. The individual loss contributions occur at distinct characteristic time constants, necessitating different measurement techniques.

Loss contributions with small- and medium-time constants, evolving at frequencies ranging from MHz to a few mHz, can be effectively isolated through EIS. Solid-state diffusion of Li within the CAM and the diffusion of Li ions within the electrolyte have large time constants in the low-frequency range, between mHz and μHz. However, conducting EIS measurements in this low-frequency range renders the system non-stationary, as the low-frequency excitation signal would either charge or discharge the cell, significantly altering the SOC. Consequently, EIS proves unsuitable for analyzing diffusion processes under these conditions. For these reasons, a time-domain measurement based on pulse measurements emerges as the preferred method. A succinct overview of the combined application of these methods is provided below.

High and middle frequency losses.—The electrochemical impedance associated with individual loss processes and their parameter dependencies were deduced by fitting Nyquist plots using an equivalent circuit model (ECM) illustrated in Figs. 1a and 1b. In this model, $R_{0,cathode/E}$ embodies the sum of ohmic resistances originating from the cell hardware, the connection between the circuit board, PAT-core cell, and within the electrolyte-filled pores of the working electrode. R_{film}//CPE_{film} signifies the impedance for Li diffusion in the solid electrolyte interface of the CAM, and R_{ct}//CPE_{ct} represents the impedance for surface charge transfer.

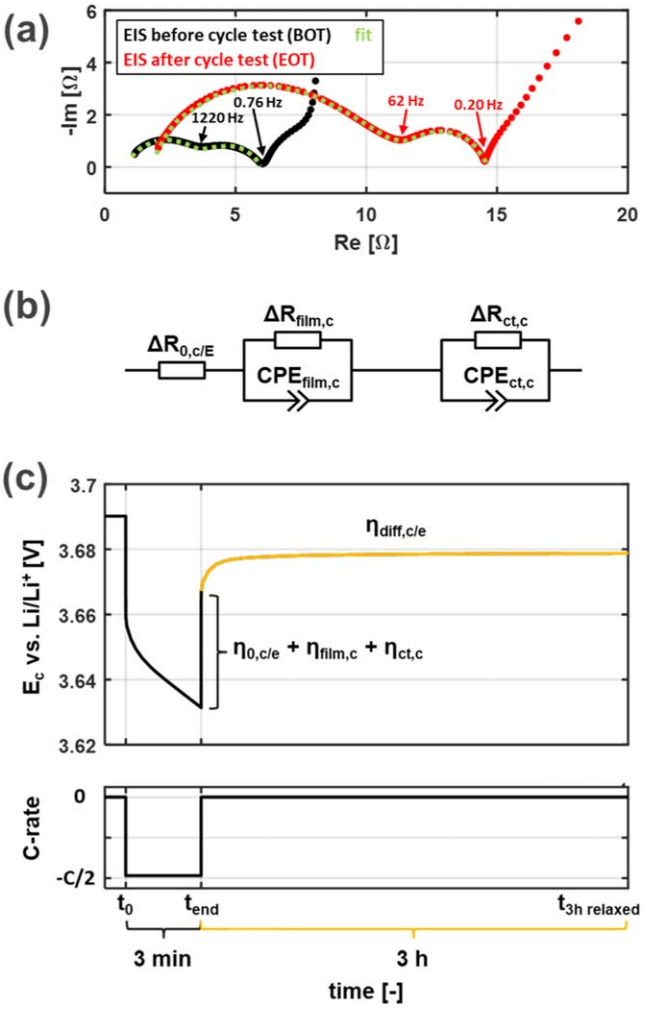

Figure 1. Illustration of the approach employed for quantifying individual loss processes in the working electrode, representing an NMC811 cathode in this study. (a) Impedance measured before and after the test via the reference electrode, (b) equivalent circuit model for the cell, (c) extraction of $\eta_{diff,c/e}$ from time-domain measurement measured via the reference electrode.

Low frequency losses.—By subjecting the cell to a constant current pulse, all loss processes are activated, resulting in the accumulation of the total overpotential η. Upon discontinuation of the current, the cathode potential E_c relaxes to E_c^0, with the difference constituting the sum of all overpotentials. The high and medium frequencies, determined by EIS, relax within seconds, followed by the slower diffusion processes. The diffusion overpotentials are then

Table I. Overview of the test descriptions of the test series with specific questions: (I) cycle dependency (baseline), (II) current rate dependence, (III) state of charge (SOC) dependency, (IV) temperature dependence.

Test profile	Leading question	Number of cycles	Current rate	Temperature	Charging protocol
I (baseline)	Cycle dependency	0, 1, 5, 10, 50, 100, 150, 200	C/2	25 °C	CC-CV
II	Current rate dependency	100	1C, 2C, 5C	25 °C	CC-CV
III	Charging protocol	200	C/2	25 °C	CC
IV	Temperature dependency	100	C/2	50 °C	CC-CV

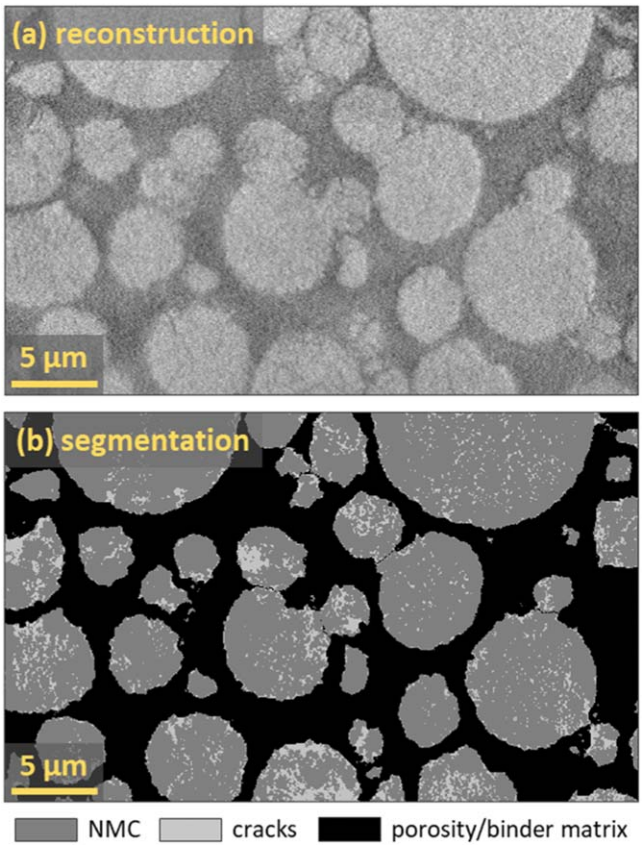

Figure 2. (a) Excerpt of a 2D slice of the 3D-reconstruction of a cathode showing particles with varying crack densities. (b) Segmentation and analysis procedure yields NMC phase, cracks, porosity and binder matrix; current collector not depicted in the excerpt.

derived by subtracting the losses at EIS-high/medium frequencies from the total overpotential. As depicted in Fig. 1c, only the loss contribution of diffusion in the solid and electrolyte to the overpotential $\eta_{\mathrm{diff,c/e}}$ remains. Consequently, the diffusion resistance $R_{diff,c/e}$ is calculated using the following formulas:

$$R_{diff,c/e} = \frac{\eta_{\mathrm{diff,c/e}}}{I} \quad [4]$$

For simplicity, $R_{diff,c/e}$ can be calculated as the difference between R_{DCIR} and the resistance components of fast loss processes quantified using GEIS and the ECM model.

$$R_{diff,c/e} = R_{\mathrm{DCIR}} - R_{0,c/e} - R_{film,c} - R_{ct,c} \quad [5]$$

For this measurement step, a 3 min constant current discharge with a C-rate of -C/2 was conducted, followed by a three-hour idle period. The relaxation phase of the voltage over 3 h after the current signal is utilized to calculate the pulse, considering that there is no change in SOC during this period, and the most relevant loss processes have subsided (see Fig. 1c).

Quantification of the change in loss processes.—The use of PAT-core cells in combination with circuit boards in the PAT-Tester-i-16 to connect the cells makes cabling obsolete. This configuration establishes a standardized cell assembly and contacting interface for the tester, ensuring consistent influences throughout the experiment. Changes in electrochemical performance parameters, derived from characterization data before (BOT; begin of test) and after (EOT; end of test) the cycling test—such as the increase in AC impedance and DC resistance—can be directly linked to cell aging effects.

To exclusively focus on changes induced by aging in the individual loss processes denoted by R_0, R_{film}, R_{ct} and R_{diff}, the respective calculated resistance values before the cycling experiment R_i^{BOT} are subtracted from the resistance values after the cycling experiment R_i^{EOT}(Eq. 6). The resulting delta ΔR_i of the considered loss process i represents the change in resistance attributed to the experiment. This methodology facilitates a direct comparison of individual loss processes across different samples from time series tests, as the respective offset is subtracted, considering only processes relevant to the aging analysis perspective.

$$\Delta R_i = R_i^{EOT} - R_i^{BOT} \quad [6]$$

Nano X-ray computed tomography imaging.—Nano X-ray computed tomography (nano-XCT) was employed to examine cathode samples in different aging states to analyze the formation of cracks within the CAM particles. The specific preparation procedure for the samples has been comprehensively detailed in our previous publication, where it can be referred to for a more in-depth overview.[45] The identical preparation protocol was followed for all samples in the current study. The samples underwent scanning using a laboratory-based X-ray microscope (Xradia, nano-XCT-100, Xradia Inc., Pleasanton, CA, USA) operating at a photon energy of 8 keV in absorption contrast mode. These X-ray CT scans, covering the region from the cathode current collector to the separator interface, possessed a high resolution of 63.5 nm/voxel, enabling detailed examination of the electrode morphology. A comprehensive dataset of 801 images over a 180° range was collected for subsequent tomographic reconstruction. The reconstruction process was executed using Tomo3D image processing software.[46] This approach facilitated the acquisition of precise insights into the three-dimensional microstructure of the electrodes, essential for a thorough understanding of the structural changes within CAM particles occurring during different aging states.

Imagine processing.—The three-dimensional reconstruction data of the actual electrode was segmented and classified to the material classes: “CAM,” “metal current collector,” and “low density” using ImageJ software[47] in conjunction with the Trainable Weka Segmentation plugin.[48] The signal-to-noise ratio in laboratory-based nano-XCT is generally recognized to be less favorable compared to synchrotron nano-XCT or conventional micro-CT due to inherent setup limitations. However, for image assessment, the contrast-to-noise ratio (CNR) is more relevant, quantifying the signal separation between foreground (CAM) and background relative to noise. Defined as $CNR = \frac{(signal_A - signal_B)}{std.deviation_B}$, this metric provides a robust measure. In our tomography data, the CNR between the CAM segment class and the interparticle volume class (excluding foil, and air) is approximately 2. Segmentation was performed using two distinct thresholds to differentiate between CAM and “low density” materials. Of the two resulting datasets, the first (A) aims to completely capture the nearly spherical CAM particles, whereas the second (B) additionally classifies the low grey value differences in the cracks as “low density” material. Contacting CAM particles were separated and labelled by a 3D watershed algorithm so that the almost spherical particles can be analyzed individually. Based on the given volume of each particle, an ideal spherical geometry was assumed to determine the equivalent radius (referred to as “particle radius”). For the resulting individual CAM particles, the crack density is then characterized in terms of their location (distance from the collector) and their size (volume). The methodology for determining crack density follows the approach outlined by Westhoff et al.,[49] utilizing the difference between segmentations A and B as the initial set of candidate voxels. These voxels were then classified and annotated with specific labels for

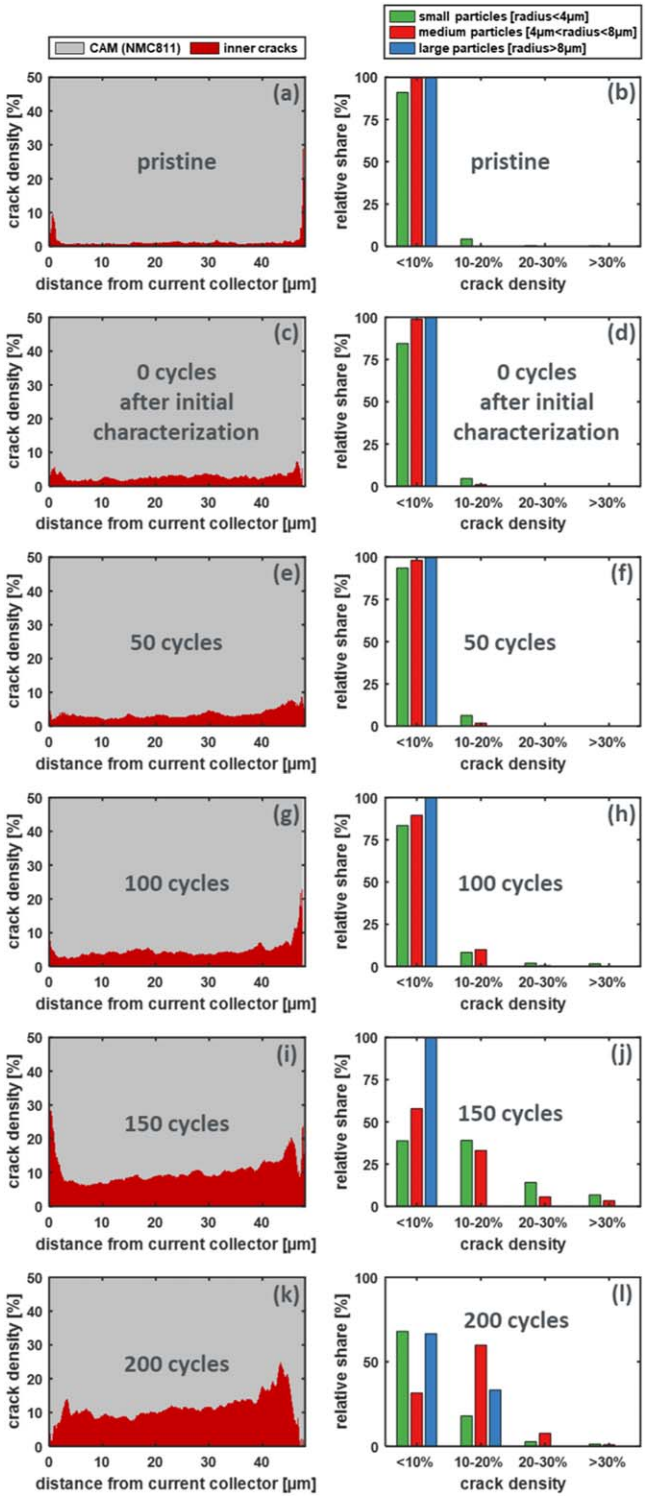

Figure 3. Crack density distribution in the CAM across electrode thickness (figures on the left) and with respect to particle size (figures on the right) during cycling aging at a C-rate of C/2 at 25°C (profile I). Samples shown: (a)-(b) pristine electrode, (c)-(d) after initial characterization, (e)-(f) after 50 cycles, (g)-(h) after 100 cycles, (i)-(j) after 150 cycles and (k)-(l) after 200 cycles.

cracks and porosity, as illustrated in Fig. 2. This approach allows for spatially resolved quantification of morphological changes in CAM particles post-cycling, facilitating detailed analysis of defects throughout the electrode thickness and at the particle level, considering both particle size and location.

Results and Discussion

In the subsequent section, we delve into the analysis and comparison of the outcomes derived from the test series detailed in Table I. Profile I examines the development of degradation throughout cycling, while Profile II compares the degradation after 100 cycles at different C-rates. Additionally, we analyze the impact of both C-rate and cumulative charge throughput by comparing Profile I and II. Moreover, the influence of the charging protocol, specifically with and without a constant voltage phase at the upper cut-off potential, is assessed through the comparison of Profile I and III. Finally, we delve into the discussion of the effects stemming from elevated temperatures during cyclic operation, comparing Profile I and IV.

Aging over cycle life.—The impact of cycle history on crack behavior is methodically examined using the snapshot logic approach, employing varying numbers of cycles for sample generation and subsequent structural analysis of the CAM with the structural data collected by nano-XCT. Quantification of cracks within the CAM phase is achieved by computing the ratio of voxels identified as cracks to the total sum of CAM voxels and crack voxels. Initially, we evaluate the extent of cracks within the CAM across the electrode thickness, presented in Figs. 3a, 3c, 3g, 3i and 3k as a function of the distance from the current collector. Additionally, fractures are categorized based on particle size, distinguishing small particles with a radius below 4 µm, medium-sized particles ranging from 4 to 8 µm, and large particles with a radius exceeding 8 µm (see Figs. 3b, 3d, 3f, 3h, 3j and 3l).

Figure 3a displays the crack density of a pristine sample, directly cut from an electrode sheet and never exposed to electrolyte. The crack density is notably low, approximately 1%, uniformly distributed throughout the entire electrode thickness, indicating that the electrode was only slightly calendered. A comparison of crack density among particle size groups reveals that only a negligible number of small particles exhibit a slightly increased crack density, with the majority having a crack density of less than 10% (see Fig. 3b).

Following a formation and characterization procedure, all electrode samples undergo CT scanning, with the crack density of an electrode after the initial characterization serving as the baseline for subsequent analyses (Fig. 3c). The crack density in this sample slightly increases to around 3%, maintaining uniform distribution across the electrode thickness. Examination at the particle level does not reveal significant changes at this point (see Fig. 3d).

After 50 cycles (Figs. 3e–3f), the electrode exhibits a marginal increase in crack density, with a slight slope toward the electrode-separator interface. This increase is attributed to small particles. The 100-cycle sample displays a moderate increase in crack density and gradient toward the electrode-separator interface (Fig. 3g), affecting small and medium-sized particles (Fig. 3h). This trend intensifies significantly for the 150-cycle sample, showing a substantial increase in crack density across the electrode thickness (Fig. 3i). The gradient also intensifies over the entire thickness, emphasizing an inhomogeneous distribution of CAM aging with greater intensity in the region proximate to the separator interface. At the particle level, this elevated crack density reveals a significant increase in defects for small and medium-sized particles, exceeding a 30% defect fraction. In comparison, large particles maintain a low crack density of less than 10% (see Fig. 3j).

For the 200-cycle sample, both crack density and inhomogeneity continue to increase across the electrode thickness (Fig. 3k). Peculiarities emerge at the particle level assessment (Fig. 3l). Notably, about 33% of the large particles initially show an increased crack density of 10%–20%. For medium-sized particles, the trend toward higher crack densities persists. In contrast, for small particles, there is a notable reversal, shifting toward lower crack density. This is attributed to the complete break-off of fragments from larger particles, resulting in new smaller isolated particles.

These are now considered individual small particles in the evaluation, frequently exhibiting very low crack density.

Examining the samples using a snapshot logic over a time series unveils two prominent trends: an escalating inhomogeneity in degradation across the electrode thickness towards the electrode-separator interface with increasing cycle numbers. This finding reflects prior studies,[50,51] which reported heightened crack density in CAM particles in the vicinity of the separator interface after cyclic tests. Importantly, our novel snapshot logic approach introduces a quantitative crack analysis in CAM samples with different cycle counts, enabling the evaluation of crack formation in the time series. It is noteworthy that the inhomogeneity across the electrode thickness is already detectable in a weakly pronounced form after just a few cycles, and this trend intensifies with an increasing number of cycles. This cycle life resolved assessment expands the knowledge base from the existing literature, which typically relies on comparisons between pre- and post-cycle testing. Furthermore, employing snapshot logic, we demonstrate that smaller particles exhibit a notably faster and more substantial formation of cracks compared to larger particles. Although our initial study hinted at these distinctions through a before-and-after comparison, our comprehensive time-series analysis now solidifies the finding that smaller particles are predisposed to cracking after only a few cycles, while their larger counterparts withstand such structural changes over a more extended cycling period.[45] This intriguing observation challenges the expectation that larger particles would display more noticeable damage, which conventional is attributed to their significant volume changes during cycling and their elevated tensile strength at fracture. Qualitatively, an increase in particle radius is associated with a decrease in tensile strength.[52] However, this relationship does not account for the inhomogeneous loading resulting from inhomogeneous lithiation at moderate C-rates during battery operation. Consequently, this correlation alone is insufficient to adequately explain the observed cracking behavior under the various operating conditions examined in this study. The counter-intuitive finding, where smaller particles exhibit more cracking, can be explained by considering their higher surface-to-volume ratio compared to larger particles. This higher ratio results in a greater cumulative charge throughput over the cycle life for small and medium-sized particles. The smaller particle radius facilitates faster Li diffusion from the particle surface to its core. In contrast, large-sized particles may experience steep Li concentration gradients due to the extended diffusion path from the surface to the core. This gradient causes the outer regions of the particle to undergo more intense lithiation and delithiation during cycling compared to the core, leading to significantly lower cumulative charge throughput per unit volume at the core and potentially reduced internal stress for large particles.[53] Over the cycle life, the less lithiated core in large particles may lead to higher active material utilization across the entire particle volume in small and medium-sized particles, increasing cumulative stress and, consequently, resulting in more significant cracking for the small and medium side particles. To the best of our knowledge, this insight has not been previously presented in the literature.

Figures 4a–4h shows the dynamic evolution of electrochemical performance parameters over cyclic aging. The capacity evolution over cycling number in Fig. 4a reveals for all cells a stable discharge capacity in the initial 50 cycles, followed by a gradual decline up to 100 cycles. A substantial capacity drop becomes evident between 100 and 200 cycles.

Figure 4b compares the discharge capacity at C/20 and C/2 after cyclic aging with the initial discharge capacity at C/20. The capacity retention at C/20 contains negligible overpotentials and capacity losses are therefore attributed to loss of active Li storage sites, changes in overpotentials due to aging can be observed for C/2. The 50-cycle sample exhibits increased irreversible capacity loss, possibly stemming from active material loss due to particle cracking. Furthermore, the difference between C/20 and C/2 discharge capacity diminishes for the 50-cycle sample, indicating that overpotential losses from previous cycles transform into non-usable capacity. Particle cracking might trigger this effect, leading to an increased CAM-to-electrolyte interface area, favoring charge transfer and temporarily reducing overpotential until the newly formed surface area is passivated by side reactions. In samples subjected to over 100 cycles, a widening disparity between the discharge capacities at C/20 and C/2 rates is evident, indicative of a diminishing rate capability.

An investigation into the transformation of the initial layered NMC structure of the CAM to the rock salt phase at the particle surface during cycling requires a detailed analysis of charge-discharge curves at C/20 after cycle testing. The derivatives of these curves, presented in the dQ/dE analysis in Fig. 4c, offer valuable insights into the phase transitions occurring at the CAM surface. As Li deintercalates, the CAM undergoes a series of phase transitions from the original layered structure (H1) to the monoclinic phase (M) and two hexagonal phases (H2 and H3), as indicated in Fig. 4c. For samples over 50 cycles, the observed gradual decay of the peak around 4.15 V indicates that the investigated CAM suffered from an irreversible phase transformation at the CAM-to-electrolyte interface. The underlying structural instability is caused by the anisotropic lattice volume change, where oxygen release takes place during deintercalation.[15,54,55] The extent of the H2-H3 phase transition, reflected in the peak decay, correlates with the deterioration in capacity retention, a phenomenon previously observed by[3,15] and.[56] Notably, our study introduces the first direct relationship between the peak decay in the region of the H2-H3 phase transition and the quantitatively determined crack density within the CAM.

The phase transitions in Ni-rich NMC serve as a diagnostic indicator for determining the absolute state of charge, as previously demonstrated by.[57] Minima observed in the dQ/dE profiles in Fig. 4c correspond to single-phase regions resulting from Li ordering states. Analyzing the dQ/dE minimum related to the monoclinic phase (M) throughout the cycle life allows the calculation of lithium content in NMC at both end-of-charge and end-of-discharge. This calculation enables the differentiation of capacity loss occurring at high and low states of charge, corresponding to low and high Li content, respectively. Figure 4d illustrates the determined Li contents of the CAM at end-of-charge and end-of-discharge over cycle life. After 100 cycles, a trend emerges in the plots revealing a narrowing effective SOC window due to increasing losses in full and empty state during cycling, a phenomenon previously reported for LNO[57] and for NMC cathodes.[58] The degree of lithiation achieved at the lower end of the discharge is notably more limited compared to the upper end in the charging direction. The narrowing of the effective state of charge window over cycles aligns with the decrease in the characteristic H2-H3 peak observed in Fig. 4c for the respective number of cycles. This phenomenon is ascribed to resistance accumulation, which we will dissect into individual loss processes in the subsequent section for detailed analysis. During charging, the CV phase at the upper end voltage, which is terminated when cut-off current of C/20 is reached, helps to reduce concentration gradients from the CAM particle surface to the core, even at elevated overpotentials. Conversely, during CC discharge, the process terminates immediately upon reaching the lower cut-off voltage, resulting in increasing concentration gradients at the end of discharge over cycle life due to resistance build-up and the absence of the CV phase. This limitation results in a reduced utilization of lithium storage sites in discharge direction and a subsequent reduction in the state of lithiation.

Impedance and time domain half-cell measurements were conducted both before and after the cycle tests to decipher the processes contributing to overpotential losses. In Figs. 4e–4h, the identified resistance values displayed as deviations from the initial resistance values of the respective cell, determined prior to the cycling test, are plotted against the cumulative throughput.

Initially, ohmic and ionic resistances show only marginal increases up to around 100 cycles (ΔR_0, Fig. 4e). Beyond 100 cycles, coinciding with a sharp increase in crack density, both ohmic

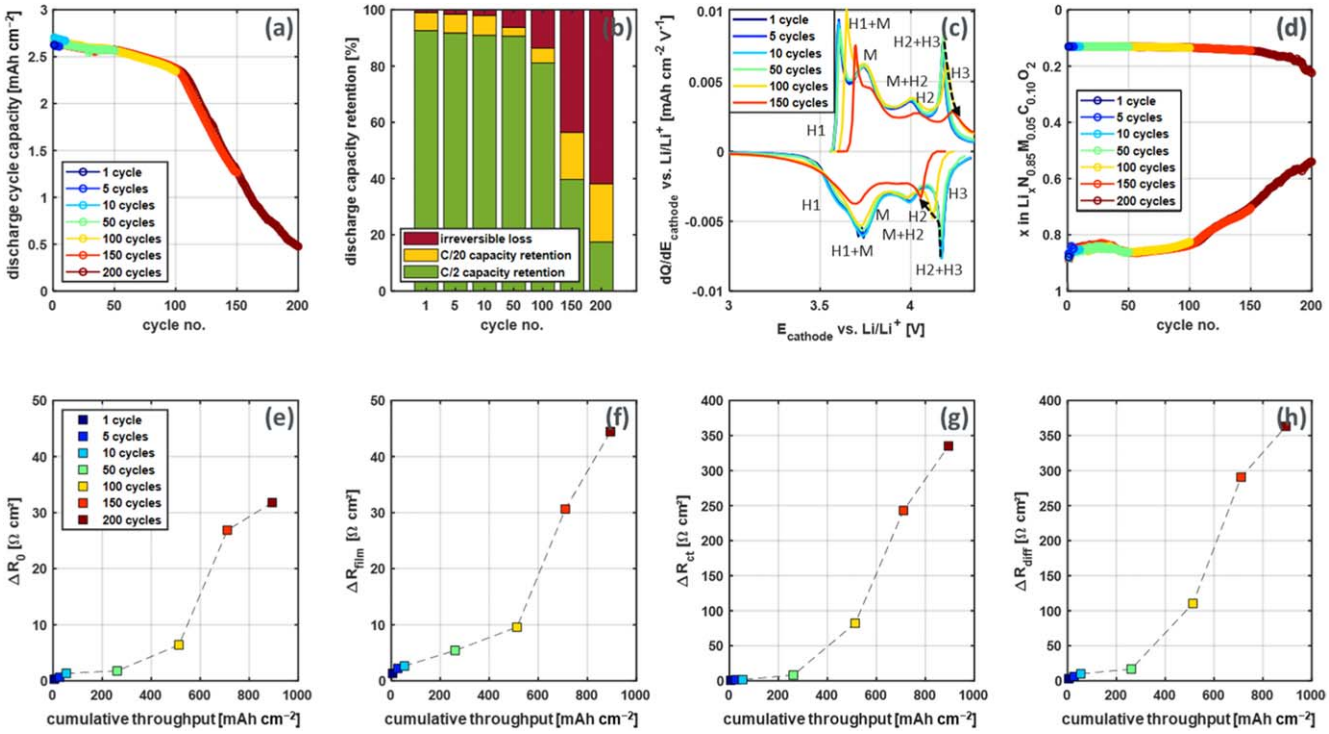

Figure 4. Overview of the individual cycle experiments with a C-rate of C/2 up to 200 cycles at 25 °C (profile I): (a) C/2 cycle discharge capacity, (b) discharge capacity retention at different C-rates and irreversible capacity loss, (c) Differential Capacity Analysis (dQ/dE) measured at a C-rate of C/20, (d) Estimated lithium content at end-of-charge and at end-of-discharge calculated from a dQ/dE analysis, (e) ΔR_0 ohmic and ionic resistance, (f) ΔR_{film} impedance for Li diffusion in the solid-electrolyte interface, (g) ΔR_{ct} impedance for surface charge transfer, (h) ΔR_{diff} NMC and electrolyte diffusion resistance.

and ionic resistances exhibit substantial increases. We attribute this to cracking-induced changed pathways for the charge species: On the one hand, the extensive formation of cracks in the CAM particles can provoke electrical disconnection between the CAM and the carbon binder domain, thereby elevating ohmic resistance. On the other hand, the cracks in the CAM particles could introduce additional porosity within the particles. If these cracks become filled with electrolyte due to capillary forces, the effective tortuosity in the electrode increases. During operation, this leads to extended transport paths through the electrolyte phase, consequently amplifying ionic resistance. Generally, electrode electrical resistance is very low due to the addition of conductive carbon black to the cathode material, making such losses usually negligible. As suggested by,[59] a partial detachment of particles from the carbon binder domain only has an electrically limiting effect when the detachment degree exceeds 75%. Hence, we attribute the predominant increase in ohmic/ionic losses to ionic losses arising from increased tortuosity.

As the crack density increases around 50 cycles, notable rises in CAM-to-electrolyte interface film resistance (ΔR_{film}, Fig. 4f) and cathode charge transfer resistance (ΔR_{ct}, Fig. 4g) are evident. This is likely linked to chemical and electrochemical oxidation of the electrolyte prompted by the release of reactive oxygen or electrochemical oxidation, processes elucidated in previous research.[36,37] These mechanisms are known to generate additional film layers on the fractured CAM secondary particle surfaces, introducing substantial ionic conduction resistance. Beyond 50 cycles, irreversible phase transformation initiates, accumulating a rock-salt phase NiO layer on particle surfaces (see dQ/dE analysis, Fig. 4d). This layer impedes Li (de)intercalation due to reduced ionic conductivity, resulting in a significant increase in charge transfer resistance and diffusion resistance (ΔR_{diff}, Fig. 4h). The observed deceleration in Li diffusion may also be attributed to cracks affecting effective diffusion paths along grain boundaries, slowing Li diffusion compared to pristine particles. Beginning at approximately 100 cycles, increases in ΔR_{ct} and ΔR_{diff} emerge as the predominant factors driving rate capability loss during cyclic aging; this correlates closely with the fragmentation of CAM particles (Fig. 3) and the evolution of resistivity contributions (Figs. 4e–4h).

Influence of C-rate on aging.—The series of samples in Profile II underwent a 100-cycle test at various C-rates, aiming to scrutinize the influence of C-rate on cracking within the CAM and its associated electrochemical performance parameters. The findings, illustrated in Figs. 5a, 5c, 5e, and 5g, reveal a positive correlation between C-rate and observed crack density in the CAM for all samples. It is noteworthy that, in comparison to Profile I, the development of an increased gradient across the dimension of the electrode thickness is relatively minor with rising crack density. This observation is particularly pronounced during the transition from C/2 to 2C. Interestingly, in the case of the 5C sample, despite exhibiting the highest crack density, there is no distinct gradient evident across the thickness of the electrode. Instead, it appears that the elevated crack density extends almost uniformly across the entire electrode volume. This phenomenon could be attributed to low electronic conductivity, fostering a more homogeneous particle utilization in proximity to the current collector at the comparatively high C-rate of 5C. For more moderate C-rates, up to about 2C, the prevailing theory posits that particles situated in the vicinity of the separator interface undergo a higher cumulative charge throughput. Over the course of the cycle life, this results in an increased cumulative volume change, manifesting a discernible influence on crack formation.

Across all tested C-rates, large particles consistently display lower crack density compared to small particles (see Figs. 5b, 5d, 5f and 5h). This observation corroborates the hypothesis proposed by,[53] indicating that smaller particle radii enable faster Li diffusion from the surface to the core. Conversely, larger particles may encounter steep Li concentration gradients, potentially mitigating internal stresses. This effect is anticipated to amplify at higher C-rates due to steepening Li concentration gradients with increasing rate, leading to less cumulative lithiation and delithiation per unit volume within the area of particle core. This is due to the earlier reaching of the cut-off voltage caused by overpotential, confirming our findings that the

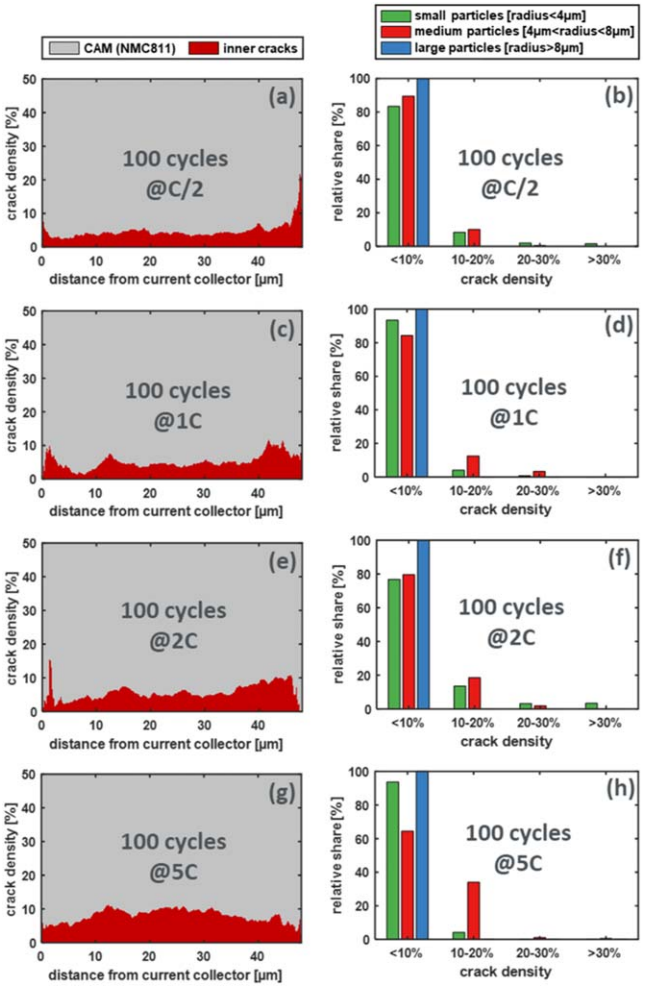

Figure 5. Crack density distribution in the CAM across electrode thickness (figures on the left) and with respect to particle size (figures on the right). Electrode samples were cycled at 25 °C for 100 cycles at a C-rate of: (a), (b) C/2, (c), (d) 1C, (e), (f) 2C and (g), (h) 5C.

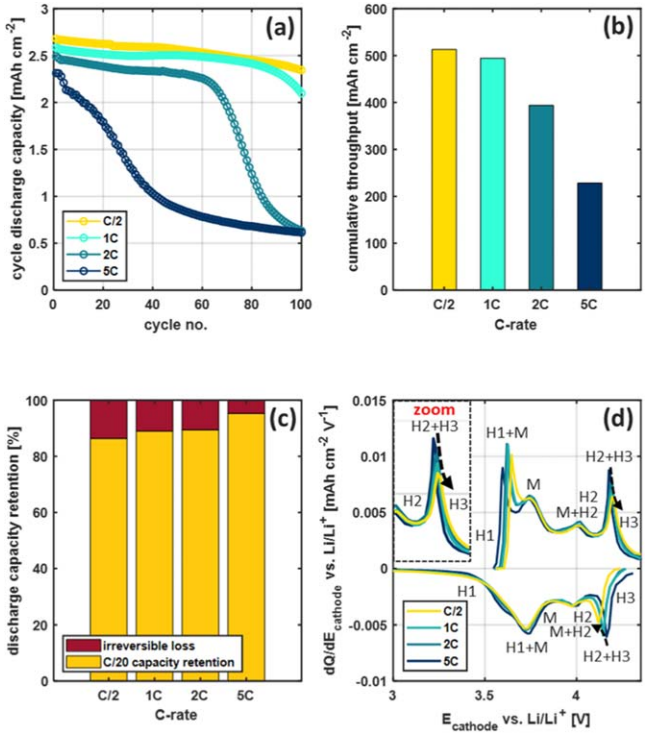

Figure 6. Electrochemical performance for cycling aging after 100 cycles at different C-rates: (a) cycle discharge capacity, (b) cumulative charge and discharge throughput, (c) discharge capacity retention vs irreversible capacity loss, (d) Differential Capacity Analysis (dQ/dE) measured at a C-rate of C/20.

crack density in large particles does not significantly increase with rising C-rates.

In Fig. 6a, the discharge capacity over 100 cycles is depicted for various C-rates, revealing an anticipated trend: higher C-rates lead to a more pronounced decline in discharge capacity during cycling. Consequently, the overall charge throughput after 100 cycles in high C-rate experiments is lower than in experiments with lower C-rates, as illustrated in Fig. 6b. Notably, a lower cumulative charge throughput corresponds to a reduced irreversible capacity loss, irrespective of the specific C-rate in the experiment, as evident in Fig. 6c. Additionally, the dQ/dE graphs in Fig. 6d emphasize that the decline in characteristic peaks at around 4.15 V correlates with the charge throughput of the respective sample, rather than the C-rate applied. This observation is remarkable as it indicates that the irreversible phase transformation linked to the peak of the H2-H3 phase transition is associated with cumulative charge throughput rather than the applied C-rate and extend of particle cracking.

To delve deeper into the primary factors influencing degradation, we compare two samples with comparable cumulative charge throughput but substantially different C-rates. The sample at a C-rate of 5C (referred to as 100 cycles@5C), achieves a comparable cumulative charge throughput after 100 cycles as the sample cycled 50 times at a C-rate of C/2 (referred to as 50 cycles@C/2), as depicted in Fig. 7b. However, Fig. 7a reveals that the 100 cycles@5C sample experiences a rapid decline in cycle discharge capacity over the cycle test, whereas the 50 cycles@C/2 sample maintains a relatively stable pattern after 50 cycles. Surprisingly, a comparison of the discharge capacity measured at a low C-rate of C/20, where overpotentials can be neglected, shows no increased loss of capacity despite a tenfold increase in the C-rate with comparable charge throughput in the cycle test (see Fig. 7c). Furthermore, the dQ/dE plot in Fig. 7d shows an almost identical course and peak decay of the H2-H3 phase transition for both samples, along with the resistances of the loss processes (see Figs. 7e–7h). Consequently, no accelerated aging is observed in electrochemical performance parameters and phase transformation at a significantly increased C-rate. This contrasts with the substantial increased crack density observed for the 100 cycles@5C sample, which, despite creating additional CAM-to-electrolyte interface area for side reactions, does not show a direct impact on the evolution of capacity loss, resistive contributions of loss processes, or the phase transformation according to dQ/dE analysis. Thus, a significant loss of accessible CAM due to electrical disconnection caused by particle cracking appears unlikely. Instead, the observed decrease in cycle discharge capacity at higher C-rates seems to result from a general loss of rate capability in the CAM, a consequence of increased resistance making the remaining capacity more challenging to access, particularly noticeable at high C-rates. The phase transformation exclusively correlates with the cumulative charge throughput, a relationship that, to our knowledge, has not been explicitly described in the literature.

Influence of constant voltage charging procedure.—Prior research has demonstrated that increasing the cut-off potential in Ni-rich NMC-based cathodes induces particle cracking and subsequent capacity loss.[60] Concurrent research has emphasized that these elevated potentials can accelerate the surface reconstruction of NMC materials, leading to the formation of the rock salt phase NiO and a subsequent rise in charge transfer resistance.[19,32–35] In contrast, our investigation into C-rate variation revealed that an elevated crack

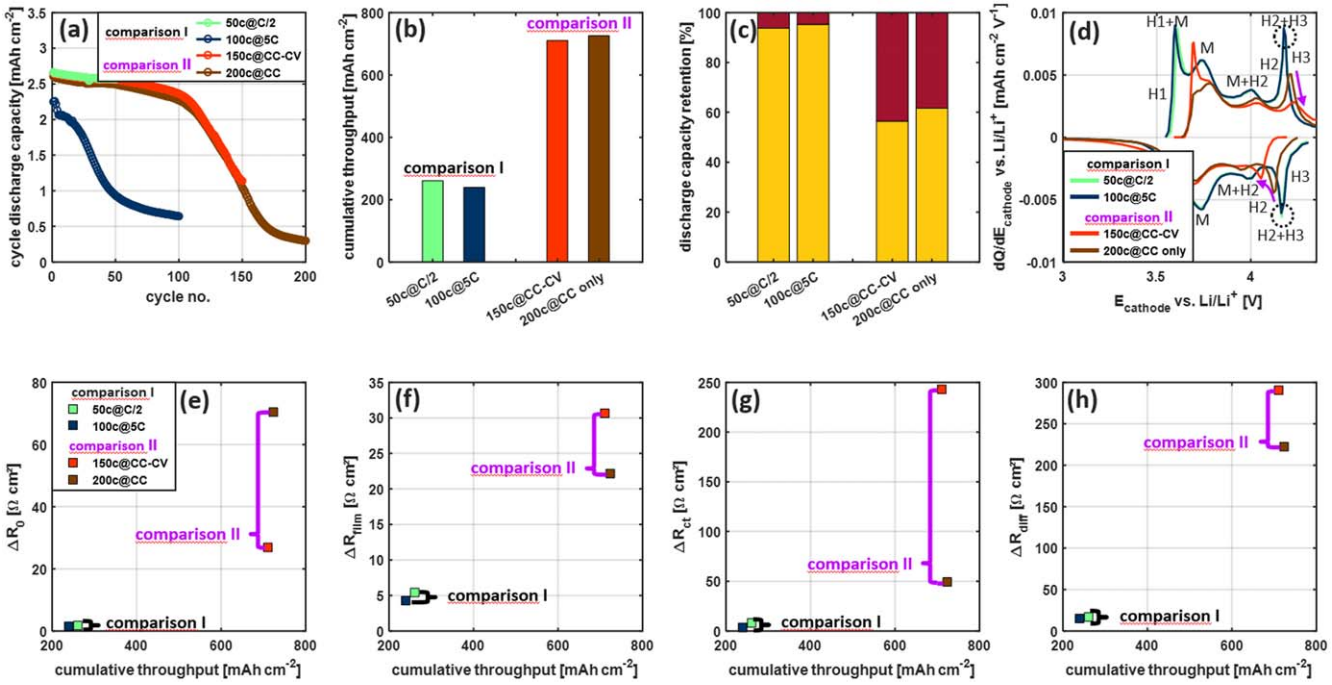

Figure 7. Comparison of experiments with different load profiles, but comparable cumulative charge throughput. 50 cycles at C/2 vs 100 cycles at 5C; 150 cycles at C/2 vs 200 cycles at C/2 without a CV phase during charge. (a) cumulative charge and discharge throughput, (b) cycle discharge capacity, (c) discharge capacity retention and irreversible capacity loss, (d) Differential Capacity Analysis (dQ/dE) measured at a C-rate of C/20, (e) ohmic and ionic resistance ΔR_0, (f) impedance for Li diffusion in the solid electrolyte interface ΔR_{film}, (g) impedance for surface charge transfer ΔR_{ct}, (h) NMC and electrolyte diffusion resistance ΔR_{diff}.

density doesn't inherently lead to diminished capacity retention. Instead, this capacity decline seams to be associated with cumulative charge throughput and dwell time at high cathode potentials due to increased loss processes. To explore this phenomenon, a cell was exclusively operated at a constant current (CC) of C/2 for 200 cycles, eliminating the constant voltage (CV) phase at the charge end. This adjustment reduced charge throughput and dwell time at high cathode potentials while maintaining the same number of cycles representing the occurrence of H2 and H3 phase transitions. This cell is referred to as the 200 cycles@CC-only sample. The cumulative charge throughput after 200 cycles with only a CC charge phase is comparable to 150 cycles at C/2 with a CC-CV phase (see Fig. 7b). In the subsequent analysis, these two cells are compared to explore the influence of the CV phase during charging. Figure 7d illustrates the dQ/dE plot, revealing a broader voltage window in the charge direction, particularly at the lower charge-end for the 200 cycles@CC-only sample, suggesting reduced kinetic limitations. Additionally, the characteristic peak of the H2-H3 phase transition around 4.15V for CC-only cells remains more prominent, indicating diminished rock salt formation. This hypothesis gains further support from the notably lower charge transfer resistance (see Fig. 7g) and lower diffusion resistance observed for the 200 cycles@CC-only sample (see Fig. 7h). Hence, eliminating the CV phase can significantly mitigate the aging of loss processes at an equivalent cumulative charge throughput. This observation likely stems from the abbreviated dwell time and diminished charge throughput at high cathode potentials, which, in turn, is presumed to curtail the formation of the rock salt phase.

The examination of CAM fracturing at the electrode level in Fig. 8a uncovers a substantial crack density in the 200 cycles@CC-only sample, surpassing that of the 150 cycles@CC-CV sample (Fig. 3i) and closely resembling the 200-cycle sample (Fig. 3k). Strikingly, akin to very high C-rate conditions, the 200 cycles@CC-only sample exhibits a uniform distribution of cracks across the electrode thickness without forming a gradient. Assessing crack distribution across particle sizes shows a more pronounced cracking

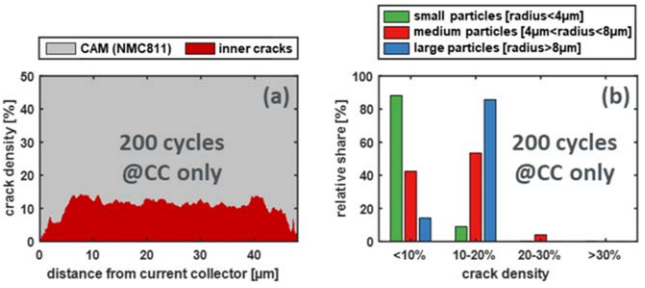

Figure 8. Crack density after 200 cycles of charging without CV phase at a C-rate of C/2. (a) Crack density across electrode thickness, (b) Crack density distribution with respect to particle size.

behavior than observed for 150 and 200 cycles@CC-CV: nearly all large particles exhibit cracks, and fragments of them seem to emerge as new particles in the small particle fraction. The comparatively high crack density throughout the electrode thickness may lead to increased ion conduction path lengths, potentially explaining the elevated ohmic/ionic resistance (ΔR_0, Fig. 7e). Interestingly, among all test profiles examined, the 200 cycles@CC-only sample exhibits a transport limitation rather than a kinetic one as the dominant loss process, setting it apart from the other profiles investigated in this study. Remarkably, the crack density exhibits a more pronounced correlation with the number of cycles, indicative of the frequency of H2-H3 phase transitions, rather than the cumulative charge throughput. At the upper end of the charging process, pronounced Li concentration gradients persist within particles, which are not reduced during a CV phase before the discharge process is initiated. This continual mechanical stress on particles persists across the electrode thickness, potentially leading to a uniformly distributed rise in crack density within the electrode.

Influence of elevated temperature.—As demonstrated by,[61] cycling at an elevated ambient temperature accelerates the

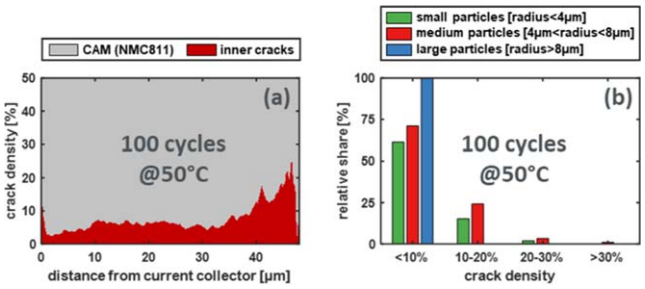

Figure 9. Crack density after 100 cycles 50 °C and C/2. (a) Crack density across electrode thickness, (b) Crack density distribution with respect to particle size.

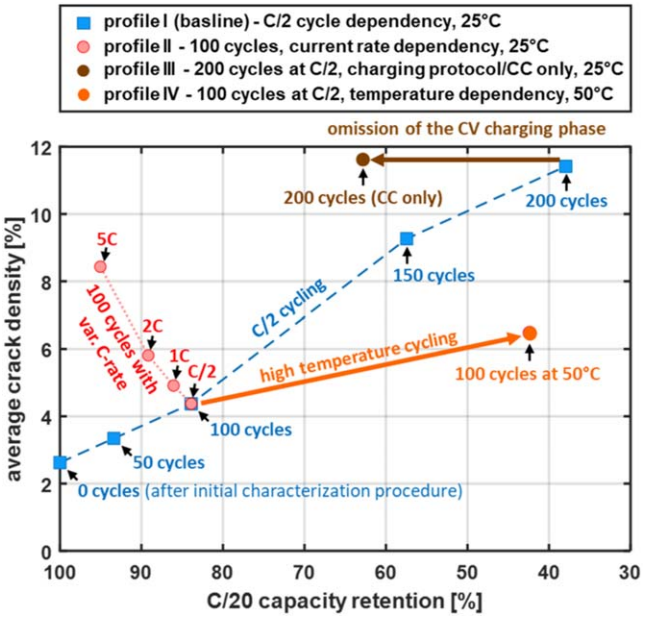

Figure 10. Comparison of all tested samples. Depiction of the average crack density in the CAM phase as a function of the C/20 capacity retention.

degradation of electrochemical performance metrics. To investigate the temperature dependence during cycling on crack formation vs electrochemical degradation, we conducted 100 cycles at C/2 at 50 °C and compared the results with the same number of cycles at 25 °C. The crack density across the electrode thickness in Fig. 9a reveals a notable increase in the 50 °C sample compared to the baseline profile with an equivalent number of cycles at 25 °C (Fig. 3a4). This increase is particularly notable in small and medium-sized particles. This quantitative analysis represents, to the best of our knowledge, the first study of the temperature dependence during cycling on crack formation within Ni-rich CAM. While the accelerated crack formation constitutes a novel finding, the observation of increased resistances and their impact on loss processes align with the findings of Refs. 37 and 61. Consequently, our electrochemical results (see Fig. S2) do not offer new insights on this matter and are thus omitted from further discussion.

Comparison of all tested samples.—To evaluate the impact of the examined operating conditions on the interplay between structural and electrochemical degradation, we juxtapose the C/20 discharge capacity retention, reflecting Li storage site retention, and the average crack density within the CAM phase of all electrode samples (see Fig. 10).

The data points highlighted in blue illustrate the evolution of average crack density within the CAM throughout cycling, using the snapshot logic from the base profile I (C/2 and 25 °C). For this profile, the measured average crack density in the CAM exhibits an approximately linear trend with the observed capacity loss.

Strikingly, as the C-rate escalates from C/2 to 1C and from 2C to 5C (for 100 cycles), there is a monotonous rise in average crack density, despite a significantly improved capacity retention. This suggests that increasing the C-rate leads to higher crack density within the CAM phase compared to the baseline cycle profile with a moderate C-rate. Intriguingly, this occurrence does not coincide with a concurrent decrease in Li storage site loss. Consequently, our findings challenge the notion that cracks in the CAM phase directly result in a loss of capacity.

Remarkably, the average crack density within the CAM after 200 CC-only charging cycles aligns closely par with that of the 200-cycle CC-CV sample. This parity exists despite a reduction in cumulative charging throughput and dwell time at high cathode potential due to the absence of the CV phase. This observation suggests that the number of cycles plays a pivotal role in CAM cracking, acting as a proxy for the occurrences of H2-H3 phase transitions. In contrast, the reduction in loss of lithium storage sites is distinctly associated with the altered dwell time and/or charge throughput at elevated cathode potentials.

Comparing the outcomes of test profiles I-III indicates that an elevated crack density does not necessarily correlate with diminished capacity retention, highlighting the significance of operational conditions. This implies that the remaining usable capacity is more likely constrained by irreversible phase transformation near the surface of the CAM particles rather than by cracking. These processes are impelled by charge throughput and dwell time at high cell voltages, as proposed by.[19,32] echo a similar opinion in their investigation of oxygen release and surface degradation in Li- and Mn-rich layered oxides, where cycle-aged samples exhibited no structural changes, indicating preserved layer structure despite oxygen release. The findings by[19] imply that the liberation of oxygen from a layered structure, a phenomenon linked to particle cracking akin to our investigation, does not promptly result in the transformation into oxygen-deficient spinel and rock salt-like phases. However,[19] observed a clear structural transformation after further 50 consecutive cycles. The increased crack density in our samples, resulting from demanding loading profiles does not necessarily hinder kinetics immediately. Nonetheless, the increased surface area due to cracks provides a foundation for further degradation through the reconstruction to spinel and rock salt-like phases, potentially requiring additional charge throughput and/or dwell time at high cathode potentials as a trigger. This aligns with the degradation of electrochemical performance parameters, contributing to the observed capacity fading. This interpretation aligns with the findings of,[35] who propose a similar degradation mechanism in their analysis of Ni-rich NMC using a combination of in situ synchrotron X-ray powder diffraction, impedance spectroscopy, and X-ray photoelectron spectroscopy.

As outlined in earlier research,[37,58] the elevation of temperature during cycling of test profile IV, a well-recognized accelerator of capacity degradation, is substantiated by our quantitative analysis, revealing a concurrent notable rise in crack density within the CAM. These results propose that subjecting cells to cycling tests at elevated temperatures provides an efficient strategy for accelerated aging tests, facilitating the swift evaluation of structural and electrochemical degradation. This holds particular significance for rapid assessments in the context of material and electrode development.

Implications for optimized electrode design and operational strategy.—Although Ni-rich NMC-based composite electrodes are a popular choice for next-generation automotive LIBs, complex degradation mechanisms continue to pose challenges in meeting performance and lifetime requirements. The subsequent sections leverage the insights gained from this study to provide recommendations for optimizing electrode design and operational strategies when utilizing Ni-rich NMC-based electrodes. The goal is to effectively

reconcile the advantages of high energy density with the imperative for an extended service life.

Notably, our findings suggest potential optimization strategies, such as replacing small poly-crystalline CAM particles prone to cracking with single-crystalline counterparts for enhanced robustness. The proposed blend of larger poly-crystalline and smaller single-crystalline particles holds the potential for enhanced resilience against cracking and the subsequent rise in resistance components under high cathode potential operation, a prerequisite for realizing the high energy density capabilities of Ni-rich NMC. An interesting research avenue could be to further refine surface coating processes for secondary particles with additional modification of the primary particles within the secondary particle matrix by coating along the grain boundaries with the aim of decoupling the CAM-electrolyte interface. In instances of particle cracking, where cracks develop along the primary particles, the additional CAM surface generated would remain decoupled from the electrolyte phase, even if electrolyte were to penetrate into the cracks. Furthermore, optimizing the primary particle coating for high ionic conductivity could enhance effective diffusion from the particle surface to the core, ultimately leading to superior electrochemical performance.

This study quantitatively demonstrates that the degradation in electrochemical performance metrics is intricately linked to dwell time and/or charge throughput at elevated cathode potentials, resulting in a subsequent loss of accessible capacity, particularly at moderate C-rates. For conserve operation of LIBs, it is imperative to minimize charge throughput at high cathode potentials throughout their entire service life. To achieve a strategy optimized for lifetime, LIBs equipped with Ni-rich NMC-based cathodes should ideally operate with a cathode potential below the H2-H3 plateau, only surpassing this limit when essential for specific use-cases, such as long-distance trips in case of automotive applications. Extended dwell times at high cathode potentials should also be avoided to prevent accelerated electrochemical loss processes. Consequently, it is advisable to charge LIBs above the H2-H3 plateau as late as possible to the subsequent discharge, aiming to minimize the time spent in the fully charged state. The critical cathode potential, situated slightly below the H2-H3 plateau, varies depending on the nickel content and decreases with higher nickel content. Implementing avoidance strategies for these detrimental conditions directly into the operational framework, coupled with user-friendly guidelines, can encourage end-users to primarily operate LIBs with Ni-rich NMC-based cathodes below the H2-H3 plateau, promoting prolonged battery lifetime.

Conclusions

This work provides a comprehensive and quantitative exploration of the structural degradation of CAM in Ni-rich layered NMC composite electrodes, shedding light on its influence on individual overpotential-causing loss processes and capacity retention. Leveraging techniques such as nano-XCT and advanced electrochemical methods, we systematically investigated the intricate interplay between structural and electrochemical degradation across various operational conditions and aging states. The insights gained from our study contribute to a more integrated understanding of the multifaceted chemical-mechanical-electrochemical failure mechanisms currently recognized in this field.

General observations across all profiles underscored the severity of particle cracking near the separator interface is particularly pronounced at moderate C-rates during charging and discharging, which is probably related to an inhomogeneous lithium concentration across the electrode thickness during cyclic operations. Additionally, the inhomogeneous degradation across different particle sizes accentuates the need to consider particle size when investigating aging behavior. This new quantitative framework is poised to guide research, facilitating an objective assessment of strategies for mitigating deterioration in Ni-rich NMC-based cathodes in terms of both electrochemical performance and mechanical integrity.

The snapshot logic approach employed, in which the number of cycles for sample generation was varied, revealed a simultaneous occurrence of particle cracking and surface degradation during normal cycling. Intriguingly, by subjecting the electrodes to more demanding charging profiles, such as increased C-rate or modified charging protocols, it was quantitatively demonstrated for the first time that crack density in the CAM induced by particle cracking significantly increased without a concurrent rise in resistance components or loss of capacity. Instead, the deterioration in electrochemical performance metrics was identified to be dependent on the dwell time or charge throughput at elevated cathode potentials. Moreover, our quantitative analysis unveiled that elevated temperatures not only expedite electrochemical aging effects but also accelerate CAM particle fragmentation, emphasizing the suitability of elevated temperatures for accelerated and comprehensive cathode material lifetime assessments.

Leveraging the insights from this study, several recommendations for optimizing electrode design and operational strategies have been proposed to balance the advantages of high energy density with the need for an extended lifetime. These include strategies such as replacing small poly-crystalline CAM particles with single-crystalline counterparts to enhance robustness against cracking. Additionally, refining surface coating processes for primary particles to decouple the CAM-electrolyte interface after particle fracture has been suggested as a promising route. Charging strategies, particularly charging as close to the subsequent discharge as possible, are crucial to minimize time spent in the fully charged state.

The quantitative framework presented in this study serves as a valuable guide for decision-making in current and future optimization initiatives for CAM in advanced material and electrode development. This marks a substantial advancement toward the commercialization of enhanced Ni-rich cathode materials, effectively balancing high energy density and prolonged battery lifetime in practical applications.

Acknowledgments

The authors acknowledge the financial support provided by Volkswagen AG and the technical realization assistance provided by Fraunhofer IKTS and EL-Cell GmbH. We also acknowledge support by the KIT-Publication Fund of the Karlsruhe Institute of Technology.

Data Availability Statements

The data presented in the manuscript are openly available in the KITopen repository at doi: 10.35097/cte6b6dzjdm30hnk.

ORCID

D. Goldbach https://orcid.org/0009-0009-0230-4482
U. Krewer https://orcid.org/0000-0002-5984-5935

References

1. B. Dunn, H. Kamath, and J. M. Tarascon, *Science*, **334**, 6058 (2011).
2. J. M. Tarascon and M. Armand, *Nature*, **414**, 6861 (2001).
3. H.-J. Noh, S. Youn, C. S. Yoon, and Y.-K. Sun, *J. Power Sources*, **233**, 121 (2013).
4. D. Andre, S.-J. Kim, P. Lamp, S. F. Lux, F. Maglia, O. Paschos, and B. Stiaszny, *J. Mater. Chem.*, **A3**, 13 (2015).
5. Y. Ding, R. Wang, L. Wang, K. Cheng, Z. Zhao, D. Mu, and B. Wu, *Energy Procedia*, **105**, 2941 (2017).
6. W. Li, E. M. Erickson, and A. Manthiram, *Nat. Energy*, **5**, 26 (2020).
7. H.-H. Ryu, K.-J. Park, C.-S. Yoon, and Y.-K. Sun, *Chem. Mater.*, **30**, 1155 (2018).
8. P. Teichert, G. G. Eshetu, H. Jahnke, and E. Figgemeier, *Batteries*, **6**, 8 (2020).
9. G. Sun, X. Yin, W. Yang, A. Song, C. Jia, W. Yang, Q. Du, Z. Mab, and G. Shao, *Phys. Chem. Chem. Phys.*, **19**, 29886 (2017).
10. Y. Xia, J. Zheng, C. Wang, and M. Gu, *Nano Energy*, **49**, 434 (2018).
11. J. Kim, H. Lee, H. Cha, M. Yoon, M. Park, and J. Cho, *Adv. En. Mater.*, **8**, 1702028 (2018).
12. J. Duan, X. Tang, H. Dai, Y. Yang, W. Wu, X. Wei, and Y. Huang, *Electrochem. En. Rev.*, **3**, 1 (2020).
13. X. Wang, Y. Ding, Y. Deng, and Z. Chen, *Adv. En. Mater.*, **10**, 1903864 (2020).
14. D.-S. Ko, J.-H. Park, S. Park, Y. N. Ham, S. J. Ahn, J.-H. Park, H. N. Han, E. Lee, W. S. Jeon, and C. Jung, *Nano En.*, **56**, 434 (2019).

15. H.-H. Ryu, G.-T. Park, C. S. Yoon, and Y.-K. Sun, *Small*, **14**, 1803179 (2018).
16. C. Yang, R. Shao, Q. Wang, T. Zhou, J. Lu, N. Jiang, P. Gao, W. Liu, Y. Yu, and H. Zhou, *En. Stor. Mater.*, **35** (2021).
17. B. Strehle, K. Kleiner, R. Jung, F. Chesneau, M. Mendez, H. A. Gasteiger, and M. Piana, *J. Electrochem. Soc.*, **164**, A400 (2017).
18. D. J. Xiong, L. D. Ellis, J. Li, H. Li, T. Hynes, J. P. Allen, J. Xia, D. S. Hall, I. G. Hill, and J. R. Dahn, *J. Electrochem. Soc.*, **164**, A3025 (2017).
19. T. Teufl, B. Strehle, P. Müller, H. A. Gasteiger, and M. A. Mendez, *J. Electrochem. Soc.*, **165**, A2718 (2018).
20. Q. Gan et al., *ACS App. En. Mater.*, **3**, 8 (2020).
21. K. Ishidzu, Y. Oka, and T. Nakamura, *Solid State Ionics*, **288**, 176 (2016).
22. H. Liu, M. Wolfman, K. Karki, Y.-S. Yu, E. A. Stach, J. Cabana, K. W. Chapman, and P. J. Chupas, *Nano Lett.*, **17**, 6 (2017).
23. J.-H. Kim, S. J. Kim, T. Yuk, J. Kim, C. S. Yoon, and Y.-K. Sun, *ACS Energy Lett.*, **3**, 12 (2018).
24. J. Langdon and A. Manthiram, *Ener. Stor. Mater.*, **37**, 143 (2021).
25. B. You et al., *Small Methods*, **5**, 2100234 (2021).
26. W. Zeng, F. Xia, W. Tian, F. Cao, J. Chen, J. Wu, R. Song, and S. Mu, *Cur. Opin. Electrochem.*, **31**, 100831 (2022).
27. L.-d Biasi, B. Schwarz, T. Brezesinski, P. Hartmann, J. Janek, and H. Ehrenberg, *Adv. Mater.*, **31**, 26 (2019).
28. H.-H. Ryu, K.-J. Park, C. S. Yoon, and Y.-K. Sun, *Chem. Mater.*, **30**, 3 (2018).
29. K.-J. Park, J.-Y. Hwang, H.-H. Ryu, F. Maglia, S.-J. Kim, P. Lamp, C. S. Yoon, and Y.-K. Sun, *ACS Energy Lett.*, **4**, 6 (2019).
30. X. Liu, X. Zhan, Z. D. Hood, W. Li, D. N. Leonard, A. Manthiram, and M. Chi, *J. Mater. Chem. A*, **9**, 2111 (2021).
31. L. Hartmann, L. Reuter, L. Wallisch, A. Beiersdorfer, A. Adam, D. Goldbach, T. Teufl, P. Lamp, H. A. Gasteiger, and J. Wandt, *J. Electrochem. Soc.*, **171**, 060506 (2024).
32. F. Lin, I. M. Markus, D. Nordlund, T.-C. Weng, M. D. Asta, H. L. Xin, and M. M. Doeff, *Nature Com.*, **5**, 3529 (2014).
33. S. Sallis et al., *Appl. Phys. Lett.*, **108**, 263902 (2016).
34. D. Streich, C. Erk, A. Guéguen, P. Müller, F.-F. Chesneau, and E. J. Berg, *J. Phys. Chem. C*, **121**, 25 (2017).
35. F. Friedrich, B. Strehle, A. T.-S. Freiberg, K. Kleiner, S. J. Day, C. Erk, M. Piana, and H. A. Gasteiger, *J. Electrochem. Soc.*, **166**, A3760 (2019).
36. Y. Qian, P. Niehoff, M. Börner, M. Grützke, X. Mönnighoff, P. Behrends, S. Nowak, M. Winter, and F. M. Schappacher, *J. Power Sources*, **329**, 31 (2016).
37. S. Liu, J. Su, J. Zhao, X. Chen, C. Zhang, T. Huang, J. Wu, and A. Yu, *J. Power Sources*, **393**, 92 (2018).
38. J. V. Laveda, J. E. Low, F. Pagani, E. Stilp, S. Dilger, V. Baran, M. Heere, and C. Battaglia, *ACS Appl. Energy Mater.*, **2**, 10 (2019).
39. D. Y. Kim, I. Park, Y. Shin, D.-H. Seo, Y.-S. Kang, S.-G. Doo, and M. Koh, *J. Power Sources*, **418**, 74 (2019).
40. R. Zhao, J. Liang, J. Huang, R. Zeng, J. Zhang, H. Chen, and G. Shi, *J. Alloys and Compounds*, **724**, 1109 (2017).
41. P. Hou, J. Yin, M. Ding, J. Huang, and X. Xu, *Small*, **13**, 45 (2017).
42. R. Du, Y. Bi, W. Yang, Z. Peng, M. Liu, Y. Liu, B. Wu, B. Yang, F. Ding, and D. Wang, *Ceram. Intern.*, **41**, 5 (2015).
43. G.-T. Park, H.-H. Ryu, N.-Y. Park, C. S. Yoon, and Y.-K. Sun, *J. Power Sources*, **442**, 227242 (2019).
44. S. Gantenbein, M. Weiss, and E. Ivers-Tiffée, *J. Power Sources*, **379**, 317 (2018).
45. D. Goldbach, J. Gluch, T. Graf, M. Gaus, S. Käbitz, M. Zillmer, and U. Krewer, *ChemElectroChem*, **10**, 20 (2023).
46. J. I. Agulleiro and J. J. Fernandez, *Bioinformatics*, **27**, 582 (2011).
47. J. Schindelin, I. Arganda-Carreras, E. Frise, V. Kaynig, M. Longair, and T. Pietzsch, *Nat. Methods*, **9**, 676 (2012).
48. I. Arganda-Carreras, V. Kaynig, C. Rueden, K. W. Eliceiri, J. Schindelin, A. Cardona, and H. S. Seung, *Bioinformatics*, **33**, 15 (2017).
49. D. Westhoff, D. P. Finegan, P. R. Shearing, and V. Schmidt, *J. Microsc.*, **270**, 1 (2018).
50. R. Xu, Y. Yang, F. Yin, P. Liu, P. Cloetens, and Y. Liu, *J. Mech. Phys. Solids*, **129**, 160 (2019).
51. Y. Yang, R. Xu, K. Zhang, S.-J. Lee, L. Mu, and P. Liu, *Adv. Energy Mater.*, **9**, 1900674 (2019).
52. J. C. Stallard, L. Wheatcroft, S. G. Booth, R. Boston, S. A. Corr, M. F. L. De Volder, B. J. Inkson, and N. A. Fleck, *Joule*, **6**, P984 (2022).
53. R. Xu, L. S. De Vasconcelos, J. Shi, J. Li, and K. Zhao, *Exp. Mech.*, **58**, 549 (2018).
54. J. Wandt, A. T. S. Freiberg, A. Ogrodnik, and H. A. Gasteiger, *Mater. Today*, **21**, 8 (2018).
55. R. Jung, M. Metzger, F. Maglia, C. Stinner, and H. A. Gasteiger, *J. Electrochem. Soc.*, **164**, A1361 (2017).
56. F. Wu et al., *Nano Energy*, **59**, 50 (2019).
57. F. Riewald, P. Kurzhals, M. Bianchini, H. Sommer, J. Janek, and H. A. Gasteiger, *J. Electrochem. Soc.*, **169**, 020529 (2022).
58. B. Rumberg, B. Epding, I. Stradtmann, M. Schleder, and A. Kwade, *J. Energy Storage*, **30**, 101510 (2020).
59. Z. Jiang et al., *Nat. Commun.*, **11**, 2310 (2020).
60. A. Aishova, G.-T. Park, C. S. Yoon, and Y.-K. Sun, *ACS Appl. Energy Mater.*, **10**, 1903179 (2020).
61. B. Strehle, F. Friedrich, and H. A. Gasteiger, *J. Electrochem. Soc.*, **168**, 050512 (2021).